Rev. Sci. Instrum. **78**, 053505 (2007); http://link.aip.org/link/?RSINAK/78/053505/1

Spatio-temporal temperature fluctuation measurements by means of a fast-swept Langmuir probe array

M. Schubert,* M. Endler,† H. Thomsen, and W7-AS Team

Max-Planck-Institut für Plasmaphysik

(Dated: received 6 February 2007; accepted 8 April 2007; published online 18 May 2007)

Abstract

Stationary Langmuir probe measurements of ion saturation current and floating potential in a plasma cannot give direct information on density and plasma potential fluctuations in the presence of temperature fluctuations. This problem can be avoided if the probe bias voltage is continuously swept faster than the fluctuation time scale, recording the current-voltage characteristic. This paper reports the development of a spatio-temporal highly resolving Langmuir probe array with 15 fast swept tips, operating in the strongly magnetised, collisionless edge plasma of the Wendelstein 7-AS stellarator [Plasma Phys. Controlled Fusion **31**, 1579 (1989)]. The probe tips are aligned in the poloidal direction, tip spacing is 2 mm, and the sweeping frequency 1.4 MHz. Current and voltage data are sampled with 50 MHz. The high bandwidth of the measurement is achieved by placing miniaturised differential amplifiers close to the probe tips in order to do an impedance transform. SMD technique and an additional inverse feedback module are utilised, allowing for an input voltage range of +/-100V, and a common mode rejection rate of 55 dB at 4 MHz, which is sufficient to resolve the nonlinear probe characteristic. For the evaluation of the data, a fit model for stationary probes is employed and found adequate. Changes of the plasma parameters during one voltage sweep are taken into account by a linear interpolation of the fit parameters. Spatio-temporal fluctuation data gained by a fast swept Langmuir probe array, which can be relevant for the turbulent radial transport of particles and energy, are presented.

*Electronic address: `Martin.Schubert@lpmi.uhp-nancy.fr`

†Electronic address: `endler@ipp.mpg.de`

I. INTRODUCTION

Langmuir probes mounted on reciprocating drives are widely used to measure fluctuations in the edge and scrape-off layer (SOL) plasma of fusion devices. Using arrays of probes, the spatio-temporal properties of plasma edge turbulence can be studied, as well as the associated anomalous transport. This probe data is an important input for numerical simulations [1–3], but also a valuable benchmark for imaging diagnostics [4]. Spatio-temporal patterns actively applied to the probes are candidates for influencing the turbulence [5]. Apart from Langmuir probes, minimal invasive techniques such as ECE imaging [6], reflectometry [7], Laser Blow-Off [8, 9], or gas puff imaging [10] exist for the visualisation of turbulence. However, as soon as the full set of transport relevant fluctuations is to be measured simultaneously, the capability of a Langmuir probe measurement is to date unsurpassed.

According to Stangeby [11] a Langmuir probe shows the characteristic for $U < U_\mathrm{f}$

$$I_\mathrm{model}(U) = -I_\mathrm{sat}\left(1 - \exp\left[\frac{e}{k_B T_\mathrm{e}}(U - U_\mathrm{f})\right]\right). \quad (1)$$

Using the vacuum vessel as the voltage reference, U_f is the probe floating voltage, and U is the actual probe voltage. Two types of fluctuation measurement schemes are frequently used: Firstly, a negative voltage bias applied to the probe for measuring the ion saturation current I_sat, which is related to the electron density n. Secondly, there is the high impedance (i.e. "floating") measurement of U_f fluctuations. This quantity is often considered as an estimate for plasma potential Φ_p fluctuations. However, for a more precise determination of Φ_p the actual electron temperature T_e and its fluctuations must be taken into account [11]. When these corrections are neglected, conflicting results can occur [12].

The temporal evolution of Φ_p, n, and T_e can be deduced simultaneously, if the probe bias voltage is actively swept faster than the timescale of the fluctuations. This method with slow sweeping is commonly used for the steady state values of Φ_p, n, T_e. During the measurement, $U < U_\mathrm{f}$ is necessary in order to avoid both the complex modification of the electron saturation current in strong magnetic fields, and capacitive hysteresis loops [13]. For a proper spatio-temporal "sampling" of the plasma fluctuations in a fusion device, the voltage sweep rate should exceed several hundred kHz, and the tip spacing should be of the order of mm. These figures are corresponding to typical values of the bandwidth of fluctuations and the correlation length perpendicular to the magnetic field, respectively [14]. Fast swept measurements have been carried out before [15–19]. There are, however, no

results published with more than 3 probe tips swept at frequencies higher than 100 kHz. The swept multi-tip array is necessary to visualise the spatial structure of electron temperature fluctuations.

We performed our measurements in the SOL plasma of the Wendelstein 7-AS stellarator (W7-AS) [20], using a poloidal array with 15 graphite tips, tip spacing d=2 mm. Typical SOL plasma properties were n=$5 \cdot 10^{18}\,\mathrm{m}^{-3}$, T_e=40 eV, and relative fluctuation levels $> 12\%$ were found. The probe location was varied within the SOL up to the last closed magnetic surface. Further inside the plasma, the tips started to emit electrons due to the thermal load, and the interpretation of the measurements became too complex.

Spatio-temporal properties of the plasma fluctuations in W7-AS deduced from I_sat and U_f data have been reported in Bleuel et al. [21]. The reported fluctuation bandwidth in the frequency domain was up to several hundred kHz with a broad shoulder around 40 kHz, while the spatial correlation length perpendicular to the magnetic field was around 1 cm. We wanted to complete this characterisation of the edge plasma turbulence by adding the spatio-temporal properties of T_e. Therefore, experiments with 15 swept probe tips with a sweeping frequency of 1.4 MHz were performed. In the following we introduce the electronic measuring technique, make a comment on the data evaluation in Sec.III, and present the plasma measurements in Sec.IV.

II. MEASUREMENT SYSTEM

A. Probe setup at W7-AS

In W7-AS the largest gradients of the plasma pressure appear perpendicular to the system of nested magnetic surfaces (see Fig. 1). The magnetic surfaces provide the thermal insulation between the plasma center, where the heating power is deposited, and the vessel wall, which is at room temperature. Turbulent plasma fluctuations tend to flatten the gradients of the plasma pressure. The dominant transport mechanism of turbulent edge plasmas has been identified in numerical simulations (e.g. [22]) as radial $E \times B$ convection caused by fluctuating poloidal electric fields. The sequence of probe tips is therefore arranged along the poloidal direction.

At W7-AS good expertise exists with the usage of small graphite cylinders as electrical probes for fluctuation measurements [21]. Graphite (also used as plasma facing component inside the vessel) has sufficient electrical conductivity and can withstand the high heat fluxes in the edge plasma. Individual tips and their electrical connections are built coaxially, so that the shielding suppresses cross-talk and ensures adequate high frequency properties. The graphite cylinder with a diameter of 0.9 mm is insulated by ceramics, leaving a length of 2 mm exposed on the plasma facing side (Fig. 2). At the opposite end it is connected to the inner conductor of a coaxial cable. The shield of that cable is connected to a stainless steel tube shielding the tip. Tip support and cables are protected by the probe head cover, which is made of insulating material boron nitride.

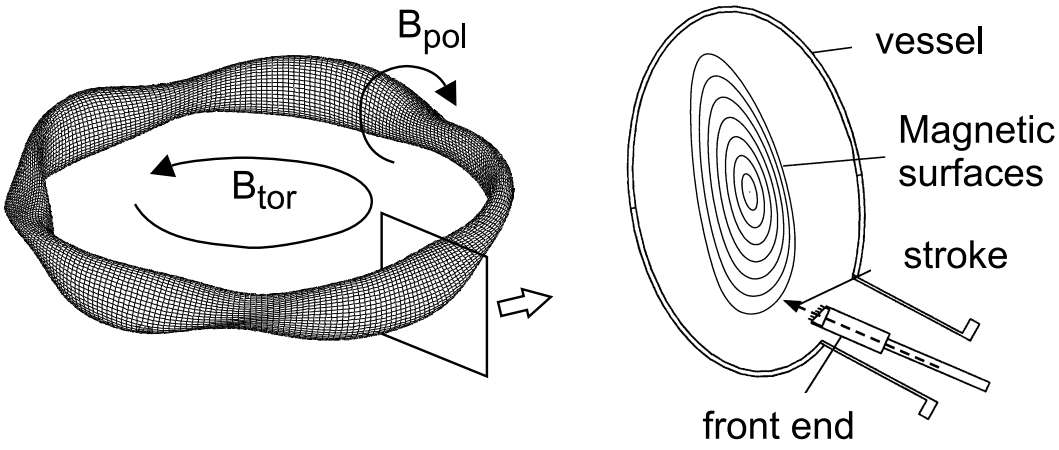

FIG. 1: Left: Closed magnetic surface of the vacuum magnetic field in the Wendelstein 7-AS stellarator (W7-AS). The magnetic field is in toroidal direction (B_{tor}) with an additional smaller poloidal component (B_{pol}). Right: Poloidal cross section showing nested magnetic surfaces and schematics of the probe system. From the lower right the probe is advanced into the vacuum vessel by a manipulator system. During plasma operation the probe head ("front end") with the 15 tip array can be brought into plasma contact by a fast reciprocation ("stroke"). The tip array is aligned along the poloidal direction.

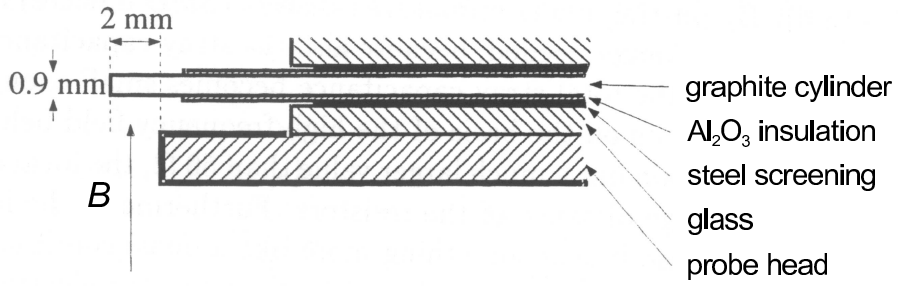

FIG. 2: Detail of the tip mounting. To produce the 15 tip array, the tip structure including insulation and screening is stacked in the direction perpendicular to the plane of this view.

B. Measuring Electronics

1. Amplifier Design

The voltage sweep peak-to-peak amplitude was 30 V, corresponding to the order of $k_B\,T_\mathrm{e}/e$. In order to keep the tip voltage below U_f, and observing in the W7-AS edge plasma that $|U_\mathrm{f}| < k_B\,T_\mathrm{e}/e$, a DC bias of -35 V was applied. A sweep frequency f_S=1.4 MHz was chosen with a sinusoidal waveform. Since the tip impedance is nonlinear and fluctuating, the bandwidth f_m of the voltage and current measurement has to be larger than f_S, our design value is f_m=10 MHz. Using one source of the biased fast sweeping voltage for all tips, and using the W7-AS vacuum vessel as the common reference potential, each individual tip current had to be measured in the tip's supply lead. In an electronic scheme where the tip current is measured by a differential amplifier as voltage across a shunt resistor, high common mode occurs with the frequency f_S at the amplifier input. Commonly available amplifiers neither have sufficient input voltage range, nor adequate common mode rejection ratio (CMRR). Both voltages at the shunt terminals were therefore divided by a factor of 10, and the common mode was actively compensated as shown in Fig. 3.

When in plasma contact, individual tip impedances are usually large compared to the 50 Ω characteristic impedance of a coaxial cable. Thus, a long cable behaves as a parasitic capacitive load, giving rise to displacement currents that must be compensated. These currents have been observed to limit the achievable bandwidth in the earlier measurements by Giannone et al. [17], who used clamp-on ammeters. A viable method to increase the bandwidth was proposed by Pfeiffer et al. [23], who also built the prototypes: Shunts and

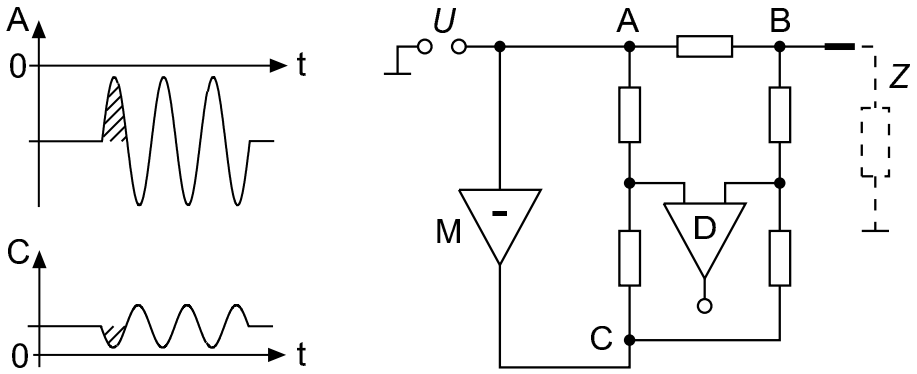

FIG. 3: Scheme of active common mode rejection. A biased high frequency signal is applied to the probe tip. Differential voltages across the shunt A-B due to plasma load Z are measured with amplifier D. The common mode is mitigated, if the module M (output into C) has a negative gain equal to the divider ratios A-C and B-C, so that both inputs of D are kept close to zero. The voltage reference is the vessel ("liner") potential. No floating amplifier, power supply or signal source are required.

miniaturised amplifier boards are placed within a cylindrical, air-vented cell directly behind the tips (Fig. 4), allowing for a short cable connection $\mathcal{O}(0.1\,\mathrm{m})$.

One amplifier board is displayed in Fig. 5. Its purpose is basically to do an impedance transform and drive a (correctly terminated) $50\,\Omega$ transmission line ending at the data acquisition. There are four channels per board, and four boards are stacked to provide measurement channels for all 15 tips, plus one modified channel that measures the common sweep voltage.

The 1/10 ratio of the voltage dividers below the terminals A and B (Fig. 5) was reproduced with a precision of $2\cdot10^{-4}$ in order to suppress the common mode signal. Using a $20\,\Omega$ shunt between A and B, we obtained 1.82 mV per 1 mA, and a precision of 1 mA up to stationary tip voltages of 100 V. Given the stray capacitance of 1 pF, the "natural" bandwidth of the upper branch of the ohmic divider (R=51 kΩ) is approx. 3 MHz. This was increased by a capacitive compensation (Fig. 5), so that settling times $t_f \approx 0.05\,\mu$s were achieved. Maximum ratings are ±0.55 A for the tip current, and ±200 V for the tip voltage.

Following the scheme from Fig. 3 the reference point C of the voltage dividers was connected to an inverted and scaled signal. To produce this, we used a two-way inverting module that could cope with up to ±100 V (output ∓10 V) in the low frequency, and ±100 V (output

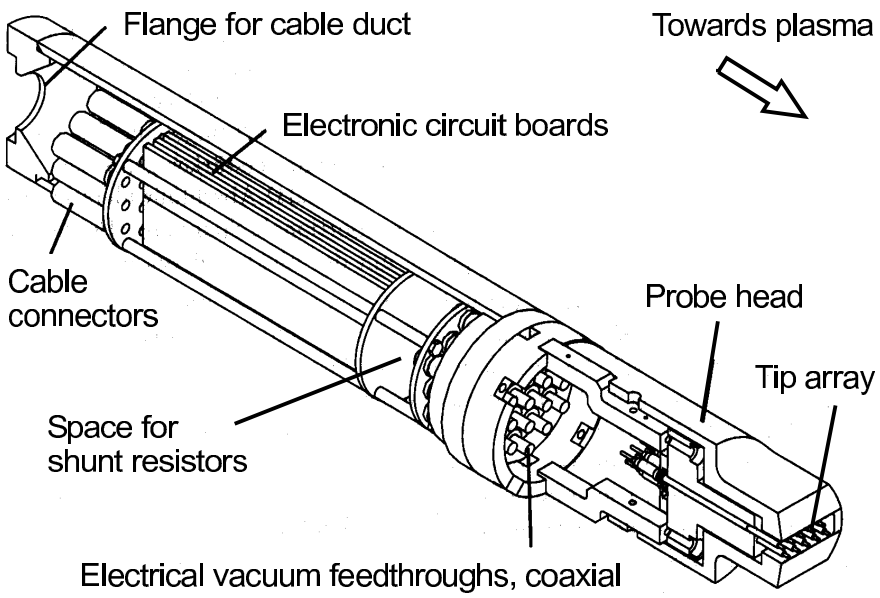

FIG. 4: Schematic of the front end in a semi-cut. On the right the plasma facing side with the graphite tips and the probe head cover are shown. The tips are coaxially connected to the feedthroughs. Behind the feedthroughs, shunt resistors and measuring electronics are mounted in a cylindrical, air-vented cell.

$\mp 10\,\mathrm{V}$) in the high frequency (HF) range. The phase of the HF was adjusted using a delay line, optimised for the sweep frequency f_S. We note that there are two stages of common mode rejection in the system: the inverted voltage signal, and the differential amplifier. A combined CMRR of $-55\,\mathrm{dB}$ was achieved at f_S=4 MHz, as shown in Fig. 6. Given the desired current precision of 1 mA this corresponds to a maximum allowable peak-to-peak sweep voltage of 11 V. Since the CMRR increases with decreasing frequency, we could use the nominal sweep amplitude of 30 V peak-to-peak at f_S=1.4 MHz. These figures, together with the input voltage range, and the compact design, are unique in present Langmuir probe electronics.

2. Peripheral Equipment

The voltage bias was generated by a DC supply ($0-125\,\mathrm{V}$, $0-10\,\mathrm{A}$), and the sweep voltage by a function generator driving a $+60\,\mathrm{dB}$ radio frequency (RF) amplifier (Model BONN BTA

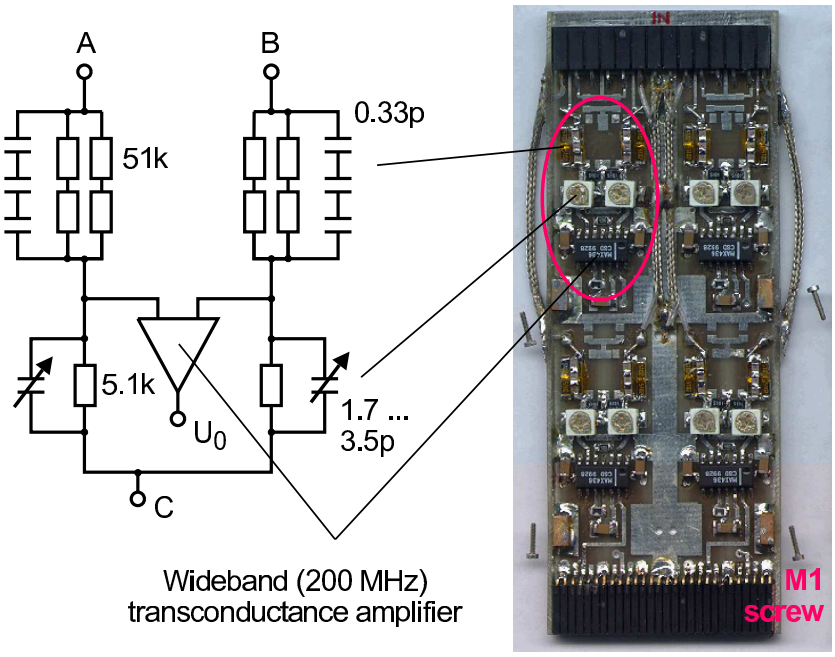

FIG. 5: Schematics and layout of the circuit boards. Left: Terminals A and B are connected to the shunt resistor, terminal C is connected to the output of the inverting module (=C in Fig. 3). SMD devices are used, including a trimming capacitor for compensation of stray capacitance. The differential amplifier, type MAX436, is operated with unity gain, and has a maximum output current of 20 mA into 50 Ω. Right: A complete board containing 4 channels. The overall dimensions are 100×40×4 mm. A top cover (not shown) with grounded inlay prevents the pick-up of HF noise from the surrounding.

0110-1000, 1 kW into 50 Ω from 10 kHz to 220 MHz). At the probe manipulator system both DC and RF were added, the module for active common mode compensation was installed, and the probe front end connected (see Fig. 7). For data acquisition two PC based transient recorders with a sampling rate of 50 MHz, 12 bit resolution, and 8 MSamples of memory per channel were used (FAST ComTec, Models Signatec PDA12/MEM500 and Spectrum MI.3024). All devices were remotely controlled, the function generator output was gated, producing the sweeping only during the acquisition time of approx. 0.168 s.

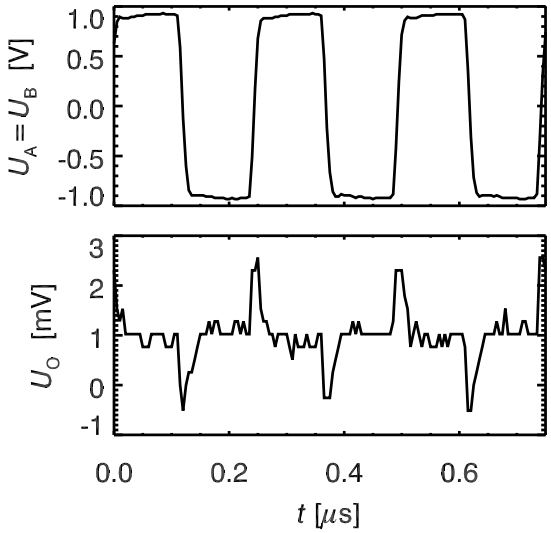

FIG. 6: Input and response of the differential amplifier to a 4 MHz common mode. Top: Signal applied to terminals A and B simultaneously. Bottom: Amplifier output. After a settling time $t_f \approx 0.05\,\mu$s the peak to peak amplitude is approx. 0.3 mV. Observing the divider ratio, the differential voltage A-B that would produce the same output is approx. 3.3 mV. Since the applied peak to peak amplitude is U_A=1.8 V, the real CMRR is $3.3 \cdot 10^{-3}\,\mathrm{V}/\,U_\mathrm{A}$ or -55 dB at 4 MHz.

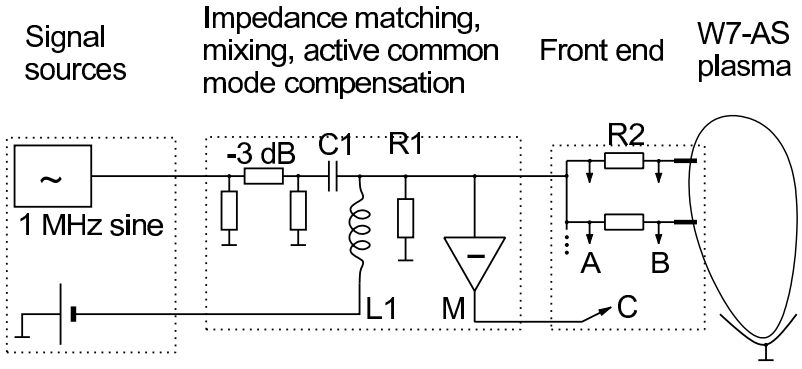

FIG. 7: Schematics of the fast sweep system. Impedance matching of the sweep signal source is improved by a -3 dB attenuator, which also damps reflections. Network: $C1$=64.7 nF, $L1$=0.22 mH, $R1$=200 Ω. The latter provides a finite impedance to plasma fluctuations with intermediate frequencies, thus preventing the voltage line between network and front end from large excursions. Amplifier M provides the active common mode compensation. $R2$=20 Ω is an exemplary shunt resistor for the tip current measurements. For the description of the front end with terminals A, B and C see Fig. 5.

III. DATA ANALYSIS

A. Fit Procedure

For each of the 15 tips the primary data are time traces $I(t_\mathrm{p})$ and $U(t_\mathrm{p})$ with a sample rate of 50 MHz (Δt_p=20 ns), as shown in Fig. 8a. Using least square fit algorithms [24], the set of the three model parameters I_sat, U_f, and T_e is obtained by using equation (1) as fit formula each half of the sinusoidal sweep period. The voltage sweep frequency of 1.4 MHz results in Δt_S=0.36 μs between subsequent values of I_sat, U_f, and T_e. Note that the average number of $I(t_\mathrm{p})$ and $U(t_\mathrm{p})$ data per sweep is equal to $\Delta t_\mathrm{S}/\Delta t_\mathrm{p}$ =18 and thus sufficiently high when compared to the model parameter count (=3).

Due to plasma fluctuations the three model parameters change in time, and the timescale of this variation is comparable to the timescale of the voltage sweep Δt_S. We can therefore expect to improve the fit quality if we account for linear changes of the model parameters between successive sweep intervals. The result of this is displayed in Fig. 8b, where we used a moving frame technique and fitted the data in packets of 12 sweeps.

Delays were found between the primary data $I(t_\mathrm{p})$ and $U(t_\mathrm{p})$ for each channel, as recorded by the ADCs. They can cause systematic differences between "up" and "down" sweeps, particularly in the model parameter U_f. One reason for such a delay is the short section of coaxial cable between shunt resistor and probe tip, which is not correctly terminated and thus causes an impedance transform. More possible reasons are uncompensated complex impedances on the electric circuit boards, and different signal delays in the integrated circuits of the differential amplifiers. To this end, the average difference of U_f between the "up" and the "down" sweeps of the entire analysis interval is evaluated after the first iteration of the fit procedure. If a systematic up-down asymmetry is found, a phase correction between $I(t_\mathrm{p})$ and $U(t_\mathrm{p})$ is applied and the fit procedure is repeated until the asymmetry vanishes. Typical time delays are within $\pm$40 ns ($\pm$2 samples). Locally in time, systematic deviations between "up" and "down" sweeps can still persist, as it can be observed in the time trace of the floating potential U_f around t=5 μs in Fig. 8b.

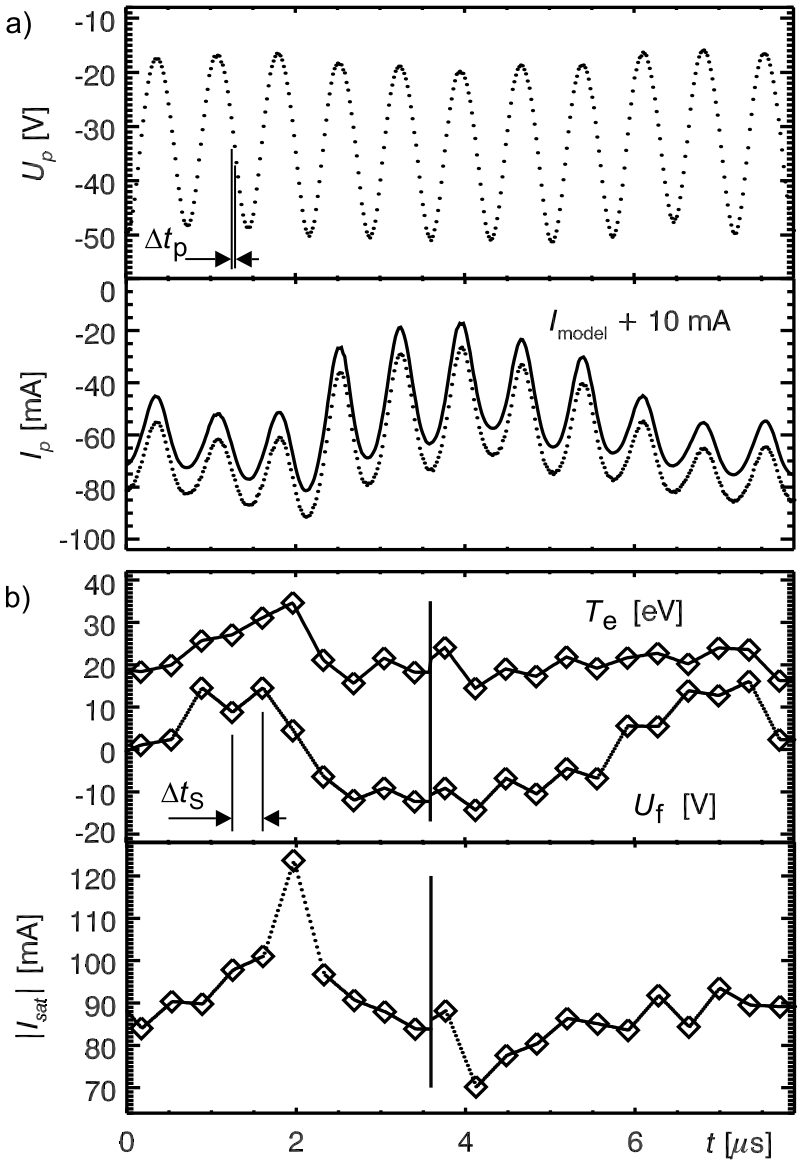

FIG. 8: (a) Primary $U(t_\mathrm{p})$ and $I(t_\mathrm{p})$ data samples, displayed using dots. (b) Corresponding model parameters $I_\mathrm{sat}(t_\mathrm{S})$, $U_\mathrm{f}(t_\mathrm{S})$, and $T_\mathrm{e}(t_\mathrm{S})$, defined each half period of the voltage sweep (diamond symbols). 12 sweeps are fitted simultaneously, and a linear interpolation on the grid t_p is performed. The boundary between two fit frames is indicated by vertical lines. The backward calculation of the probe model current according to equation (1) is overplotted in (a) with a solid line, shifted by 10 mA for better visibility.

B. Deduction of Plasma Quantities

The model parameters $I_{\rm sat}$ and $U_{\rm f}$ depend on the plasma quantities n, $\Phi_{\rm p}$, and $T_{\rm e}$. It is assumed that $T_{\rm i} = T_{\rm e}$ in the edge plasma of the W7-AS. Since the tip dimensions are small compared to the mean free paths of the plasma particles, and large compared to their gyro radii and to the Debye length, the use of theory for a classical Langmuir probe in a strong magnetic field [25] is appropriate. $I_{\rm sat}$ is thus related to the ion current density according to

$$I_{\rm sat} = 4\, r_p\, l_p \;\cdot\; j_{i,\,\rm sat}\ , \tag{2}$$

where r_p and l_p are radius and length of the cylindrical probe tip, respectively. Following calculations by Stangeby [11] yields:

$$j_{i,\,\rm sat} = 1.25 \cdot \frac{1}{2}\, e\, n \sqrt{\frac{2\, k_B\, T_{\rm e}}{m_i}}\ . \tag{3}$$

The correction factor 1.25 is based on the more detailed kinetic analysis by Emmert et al. [26], and m_i is the ion mass.

The relation between $U_{\rm f}$ and $\Phi_{\rm p}$ is given by:

$$\frac{e\,(U_p\, - U_{\rm f}\,)}{k_B T_e} = \ln\left((1-\gamma_e) \sqrt{\frac{m_i}{\pi\, m_e}} \right) - 0.22\,, \tag{4}$$

where U_p is the voltage between the unperturbed plasma potential $\Phi_{\rm p}$ and the vessel, m_e is the electron mass, and γ_e is the coefficient for secondary electron emission. The addend 0.22 is a correction due to the Emmert model [26]. For our graphite probe tips, γ_e=0.5 is assumed, which is based on the measurements by Pedgley et al. [27].

Despite the high voltage sweep frequency, stationary conditions in the probe model can be assumed [13]. Effects of the plasma sheath capacitance on the ion side are comparatively small due to perpendicular incidence of the magnetic field on the probe surface.

IV. APPLICATION AND DISCUSSION

In order to demonstrate the capability of the system, we exemplarily show the measurement result in the SOL of a W7-AS hydrogen plasma with an average magnetic field strength $B = 2.5\,\mathrm{T}$. The plasma was generated by 440 kW of electron cyclotron resonance heating (ECRH). During the stationary phase of the plasma discharge, the probe performed a reciprocation within 300 ms, and fast sweep data were recorded. Here we will discuss the average

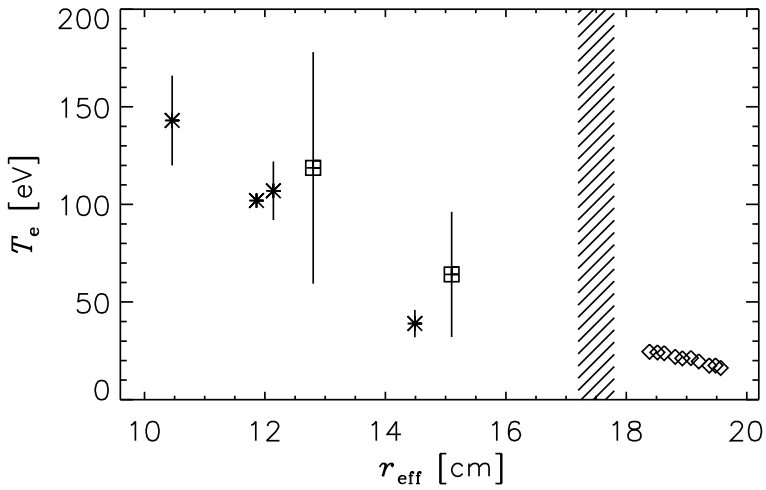

FIG. 9: Plasma electron temperature measurements in W7-AS as a function of the effective radial magnetic coordinate $r_{\rm eff}$. The data for $r_{\rm eff} > 18\,$cm are measured in the scrape-off layer by the fast swept probe system, asterisks are data points in the plasma core from the W7-AS ECE system, and squares from YAG Thomson scattering. Within the uncertainty of the data, the independent measurements yield a consistent electron temperature profile. The shaded region depicts the interface between plasma core and scrape-off layer.

electron temperature profile, the fluctuation levels, and the 2D visualisation of density and temperature fluctuations.

The average electron temperature profile in the SOL is obtained from the fit parameter $T_{\rm e}$, averaged over all tips and processed with a low pass filter. Since the heat source is located in the center of the core plasma at $r_{\rm eff}$=0 (on-axis ECRH), a monotonic decrement of $T_{\rm e}$ in direction of $r_{\rm eff}$ is expected, which is seen in the probe data (Fig. 9). Furthermore, the $T_{\rm e}$ gradient length of approx. 3 cm is of the same order as the SOL density gradient length that was published by Grigull et al. [28]. $T_{\rm e}$ is measured inside the core plasma by the independent ECE and YAG systems, see Fig. 9. When extrapolating the core and SOL $T_{\rm e}$ profiles, both coincide at the interface as expected.

The relative fluctuation level σ_{11} is defined as the standard deviation normalised to the average value, and displayed in Fig. 10. Using the square root of the sample variance in the n, $T_{\rm e}$, and $\Phi_{\rm p}$ data yields an upper limit, which does not necessarily reflect the level of plasma fluctuations, since the sample variance is enhanced by the sporadic occurrence of up-down asymmetries during the fit procedure (section III). We therefore calculate a lower

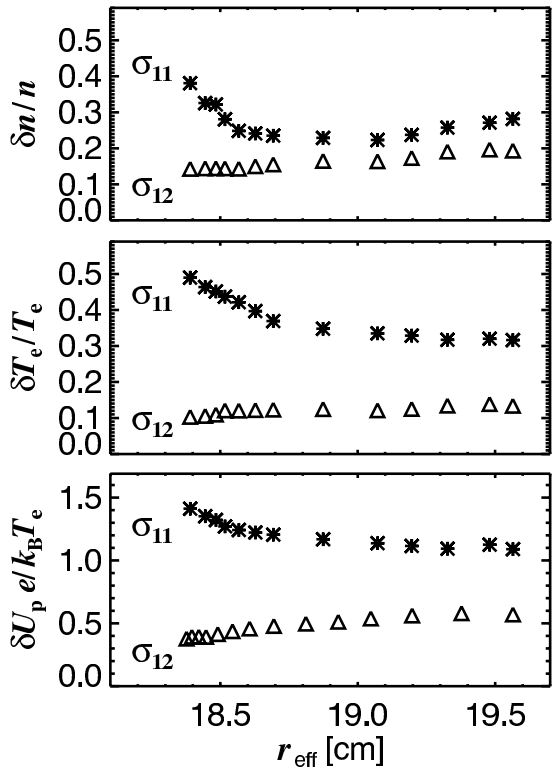

FIG. 10: Upper limit (σ_{11}, asterisks) and lower limit (σ_{12}, triangles) of the relative fluctuation level, evaluated from the sample variance, and the cross-variance on neighbouring tips (d=2 mm), respectively. T_e and n data are normalised to the average value, U_p is normalised to $k_B\bar{T}_\mathrm{e}/e$. On the x-axis the r_eff coordinate is displayed, cf. Fig. 9.

limit σ_{12} (Fig. 10) using the maximum of the square root of the cross-variance on adjacent tips x and y:

$$\sigma_{12} = \max_j \left[\sqrt{(N\bar{x}\bar{y})^{-1} \sum_i (x_i - \bar{x})\,(y_{i+j} - \bar{y})} \right] , \qquad (5)$$

where N=20000, and j is a time lag. Due to the finite propagation velocity of the fluctuation structures the maximum is usually found at a time lag $j \neq 0$. It can be assumed that σ_{12} is not affected by the up-down asymmetries, given the latter are uncorrelated on different tips. Since the correlation length of the plasma fluctuations is finite, σ_{12} however underestimates the fluctuation level. Within the uncertainty range given by σ_{11} and σ_{12}, the measurements by Giannone et al. [17] are in accordance with these results.

We show the plasma density and temperature fluctuations in contour plots as functions of time and poloidal position in Fig. 11. The fluctuation power has been equilibrated among the channels in order to compensate for different sensitivities. This visualisation compares

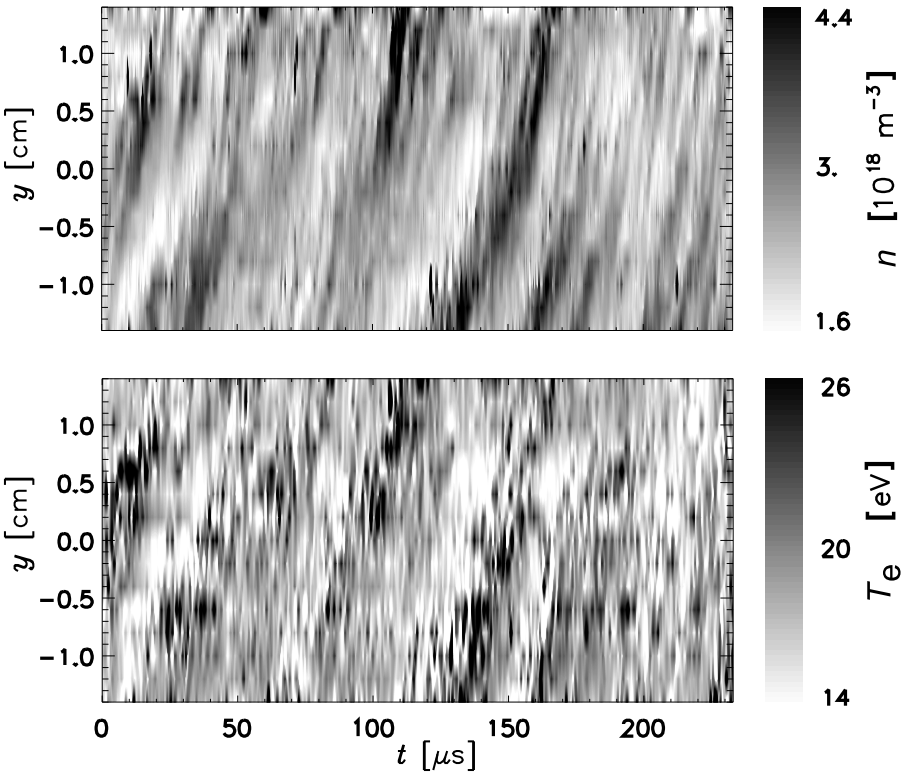

FIG. 11: Spatio-temporal evolution of plasma density (top) and electron temperature (bottom), measured with the 15 tip fast swept probe array in the scrape-off layer of W7-AS. Data spacing is 2 mm along poloidal axis y, and 0.36 μs along t. The amplitude is encoded using different shades of grey. A notch filter with the Nyquist frequency was applied to the T_e data in order to remove noise from up-down asymmetries.

well with the H_α fluctuation data from [21], but in the fast sweep data we can now clearly distinguish between plasma density and temperature, and we have a quantitative measurement. An average poloidal velocity of $7 \cdot 10^2\,\mathrm{m\,s^{-1}}$ in ion diamagnetic direction can be deduced from the inclination of the stripe patterns. Since the fluctuations intrinsically propagate in electron diamagnetic direction [22], a dominating poloidal $E \times B$ convection must be present. Considering the local magnetic field strength of 2.3 T, this corresponds to a background radial electric field $>1.6 \cdot 10^3\,\mathrm{V\,m^{-1}}$, pointing radially outward.

The varying structure sizes and structure lifetimes in Fig. 11 are typical for turbulent phenomena. For example, the large stripe visible in both density and temperature around t=140 μs corresponds to a fluctuation that enters the region of observation from y=−1.4 cm, moves along the tip array, and starts to decay at t=150 μs and $y \approx 0.5$ cm. Other structures

are "born" and grow within the region of observation like the one at $t \approx 100\,\mu$s and $y \approx 0.2\,$cm. Further analysis including the transport relevant cross relations between density, potential, and temperature is reported in [29], and will be published elsewhere.

V. CONCLUSION

This study demonstrates the simultaneous spatio-temporal measurement of T_e, n, and Φ_p fluctuations in the scrape-off layer of a fusion device by applying the voltage sweeping technique to a poloidal array of Langmuir probes. Displacement currents at high sweep frequencies in the probe tip connection lead can be mitigated using a miniaturised amplifier design that allows for an impedance transform in the probe front end. During evaluation of the probe current and voltage data it is observed that the stationary probe model is adequate in a sense, that the deviation between the measured and the fitted model data is small. Due to the high bandwidth of the plasma fluctuations, however, the fit model must take into account changes of the parameters within one voltage sweep, even at the present sweep frequency of 1.4 MHz. The application of higher sweep frequencies is desirable but very demanding due to the requirements on the differential current amplifiers.

In Wendelstein 7-AS a strong poloidal convection of fluctuation structures is found in T_e, n, and Φ_p. The structures vary in poloidal size and lifetime, as it is expected for plasma edge turbulence. Remarkably, the spatio-temporal fluctuation dimensions are similar in all fluctuating quantities. Altogether, the achieved space and time resolution have broadened the experimental view of plasma turbulence.

VI. ACKNOWLEDGMENTS

The authors wish to acknowledge the assistance of J. Ahmels, F. Beibl, H. Holitzner, M. Hron, H. Huber, A. Jenning, K.H. Knauer, W. Nagel, H. Reuter, N. Ruhs, P. Schoetz, H. Scholz, A. Schott, G. Schramm, S. Siche, and G. Zangl during setting up of the measurement system. They would like to thank H. Niedermeyer and J. Sachtleben for valuable comments.

[1] O. Garcia, V. Naulin, A. Nielsen, and J. Rasmussen, Physics of Plasmas **12**, 062309 (2005).

[2] B. Scott, Plasma Physics and Controlled Fusion **45**, A385 (2003).

[3] C. Lechte, S. Niedner, and U. Stroth, New Journal of Physics **4**, 34 (2002).

[4] J. Terry, S. Zweben, K. Hallatschek, B. LaBombard, R. Maqueda, B. Bai, C. Boswell, M. Greenwald, D. Kopon, W. Nevins, et al., Physics of Plasmas **10**, 1739 (2003).

[5] H. Thomsen, M. Endler, T. Klinger, and the W7-AS Team, Plasma Physics and Controlled Fusion **47**, 1401 (2005).

[6] S. Bäumel, G. Michel, H. Hartfuss, M. Rodriguez-Girones Arboli, and H. Hartnagel, Review of Scientific Instruments **74**, 1441 (2003).

[7] R. Nazikian, G. Kramer, and E. Valeo, Physics of Plasmas **8**, 1840 (2001).

[8] M. Bruchhausen, R. Burhenn, M. Endler, G. Kocsis, A. Pospieszczyk, S. Zoletnik, and W.-A. Team, Plasma Physics and Controlled Fusion **46**, 489 (2004).

[9] M. Bruchhausen, PhD Thesis, Heinrich-Heine-Universität Düsseldorf (2002), report Jül-3993, Institut für Plasmaphysik, Forschungszentrum Jülich GmbH, D-52425 Jülich.

[10] R. Maqueda, G. Wurden, D. Stotler, S. Zweben, B. LaBombard, J. Terry, J. Lowrance, V. Mastrocola, G. Renda, D. D'Ippolito, et al., Review of Scientific Instruments **74**, 2020 (2003).

[11] P. Stangeby, in *Physics of Plasma-Wall Interactions in Controlled Fusion*, edited by D. Post and R. Behrisch (Plenum Press, New York and London, 1986), no. 131 in NATO ASI, pp. 41–97.

[12] B. LaBombard, Physics of Plasmas **9**, 1300 (2002).

[13] P. Verplancke, R. Chodura, J. Noterdaeme, and M. Weinlich, Contributions to Plasma Physics **36**, 145 (1996), Special Issue, Proceedings of the Second International Workshop on Electrical Probes in Magnetized Plasmas.

[14] P. Liewer, Nuclear Fusion **25**, 543 (1985).

[15] P. Liewer, J. McChesney, S. Zweben, and R. Gould, Physics of Fluids **29**, 309 (1986).

[16] R. Balbín, C. Hidalgo, M. Pedrosa, I. García-Cortés, and J. Vega, Review of Scientific Instruments **63**, 4605 (1992).

[17] L. Giannone, R. Balbín, R., H. Niedermeyer, M. Endler, G. Herre, C. Hidalgo, A. Rudyj, G. Theimer, and P. Verplancke, Physics of Plasmas **1**, 3614 (1994).

[18] J. Boedo, D. Gray, R. Conn, P. Luong, M. Schaffer, R. Ivanov, A. Chernilevsky, G. van Oost, and TEXTOR Team, Review of Scientific Instruments **70**, 2997 (1999).

[19] M. Meier, R. Bengtson, G. Hallock, and A. Wootton, Physical Review Letters **87**, 085003 (2001).

[20] H. Renner, W7-AS Team, NBI Group, ICF Group, and ECRH Group, Plasma Physics and Controlled Fusion **31**, 1579 (1989).

[21] J. Bleuel, M. Endler, H. Niedermeyer, M. Schubert, H. Thomsen, and W7-AS Team, New Journal of Physics **4**, 38.1 (2002).

[22] B. Scott, Plasma Physics and Controlled Fusion **39**, 1635 (1997).

[23] U. Pfeiffer, M. Endler, J. Bleuel, H. Niedermeyer, G. Theimer, and W7-AS Team, Contributions to Plasma Physics **38**, 134 (1998), Special Issue, Proceedings of the Third International Workshop on Electrical Probes in Magnetized Plasmas.

[24] *NAG Fortran Library Mark 19*, The Numerical Algorithms Group Ltd, Oxford UK (1999).

[25] J. Laframboise and J. Rubinstein, Physics of Fluids **19**, 1900 (1976).

[26] G. Emmert, R. Wieland, A. Mense, and J. Davidson, Physics of Fluids **23**, 803 (1980).

[27] J. Pedgley, G. McCracken, H. Farhang, and B. Blott, Journal of Nuclear Materials **196-198**, 1053 (1992).

[28] P. Grigull, F. Sardei, Y. Feng, G. Herre, D. Hildebrandt, G. Kocsis, G. Kühner, and W7-AS Team, in *Tenth International Conference on Stellarators* (CIEMAT, Madrid, 1995).

[29] M. Schubert, PhD Thesis, Ernst-Moritz-Arndt University Greifswald (2005), IPP report 13/4, Max-Planck-Institut fuer Plasmaphysik, Garching, Munich.